NANO LETTERS

Letter

pubs.acs.org/NanoLett

Tunable Exciton Funnel Using Moiré Superlattice in Twisted van der Waals Bilayer

Menghao Wu, Xiaofeng Qian, and Ju Li*

Department of Nuclear Science and Engineering and Department of Materials Science and Engineering, Massachusetts Institute of Technology, Cambridge, Massachusetts 02139, United States

Supporting Information

ABSTRACT: A spatially varying bandgap drives exciton motion and can be used to funnel energy within a solid (*Nat. Photonics* **2012**, *6*, 866−872). This bandgap modulation can be created by composition variation (traditional heterojunction), elastic strain, or in the work shown next, by a small twist between two identical semiconducting atomic sheets, creating an internal stacking translation $\boldsymbol{u}(\boldsymbol{r})$ that varies gently with position $\boldsymbol{r}$ and controls the local bandgap $E_g(\boldsymbol{u}(\boldsymbol{r}))$. Recently synthesized carbon/boron nitride (*Nat. Nanotechnol.* **2013**, *8*, 119) and phosphorene (*Nat. Nanotechnol.* **2014**, *9*, 372) may be used to construct this twisted semiconductor bilayer that may be regarded as an in-plane crystal but an out-of-plane molecule, which could be useful in solar energy harvesting and electroluminescence. Here, by first-principles methods, we compute the bandgap map and delineate its material and geometric sensitivities. $E_g(\boldsymbol{u}(\boldsymbol{r}))$ is predicted to have multiple local minima ("funnel centers") due to secondary or even tertiary periodic structures in-plane, leading to a hitherto unreported pattern of multiple "exciton flow basins". A compressive strain or electric field will further enhance E_g-contrast in different regions of the pseudoheterostructure so as to absorb or emit even broader spectrum of light.

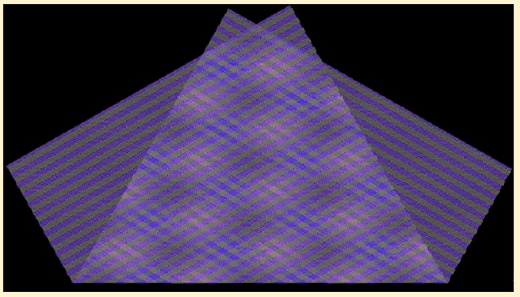

KEYWORDS: *Exciton flow basin, twisted bilayer, in-plane crystal out-of-plane molecule, pseudoheterostructure, bandgap contrast*

When two identical monolayer crystals are twisted by an angle θ, a grain boundary is created within the bilayer with a Moiré superlattice[2,4] pattern (coincidence site lattice) that can be much larger than the primitive lattice vectors $\{\boldsymbol{l}_j\}$ of the underlying monolayer, if θ is very small or near some special angles. Unlike grain boundaries in three-dimensional (3D) solids that are buried and often curved, a twisted van der Waals bilayer would be atomically flat, and importantly, optically and electronically accessible. It therefore behooves us to analyze its electronic properties carefully. Previous theoretical and experimental work have already revealed very intriguing physical properties,[5,6] including Van Hove singularities,[4] superlattice Dirac points,[4,7] Hofstadter's butterfly, and fractal quantum Hall effect.[8,9] In this work, we focus on the small-θ regime, which is experimentally achievable but not yet carefully studied. In this regime, the superlattice period $L \propto l/\theta$ may become comparable or even longer than the prevalent photon wavelength λ_{photon} and the electron mean free path Λ_{MFP}, both of which are often of the order hundreds of nanometers. In this scenario of $L \gg \lambda_{photon}, \Lambda_{MFP}$, a semiclassical phase decoherent treatment of the electron problem is warranted, where a local bandgap $E_g(\boldsymbol{r})$ may be defined as a function of the coarse-grained position $\boldsymbol{r} \equiv r_x\mathbf{e}_x + r_y\mathbf{e}_y$. Further, how the local band edges (valence band maximum VBM($\boldsymbol{r}$); conduction band minimum CBM($\boldsymbol{r}$)) are aligned is of interest for charge transport as in the chemical heterojunctions. This type of variable bandstructure material without chemical modulation may be called "pseudoheterostructure".[3]

In a previous work,[1] it was suggested that a periodic array of external clamps and indenters on a monolayer semiconductor induces an elastic strain superlattice pattern that could have interesting solar energy harvesting properties. Being a single material with a range of bandgaps $\{E_g(\boldsymbol{r})\}$, it would be similar to a chemical multijunction, which in principle can beat the Shockley−Queisser detailed-balance limit[10] of photovoltaic conversion efficiency for monobandgap semiconductors. In this work, we will show that a twisted bilayer can accomplish the same function without the burden of introducing external clamping and mechanical indentation. This self-supporting structure can generate an internal energy transport pattern called exciton funnels.[11] All it requires are high-quality semiconducting 2D monolayers, and a processing method that can control θ down to $< \sim 0.05°$.

In this work, we will model $E_g(\boldsymbol{r})$ under the following approximation. When $\theta < \sim 0.05°$, a coarse-grained "stack translation" field pattern $\boldsymbol{u}(\boldsymbol{r})$ is created (Figure 1a) that describes the relative translation between the two layers, modulo $\{\boldsymbol{l}_j\}$. $\boldsymbol{u}(\boldsymbol{r})$ satisfies $\boldsymbol{u}(\boldsymbol{r} + \boldsymbol{L}_i) = \boldsymbol{u}(\boldsymbol{r})$, giving the Moiré superlattice;[4] the amplitude satisfies $-1/2 < \boldsymbol{g}_j \cdot \boldsymbol{u}(\boldsymbol{r}) < 1/2$

Received: June 27, 2014
Revised: August 6, 2014
Published: August 11, 2014

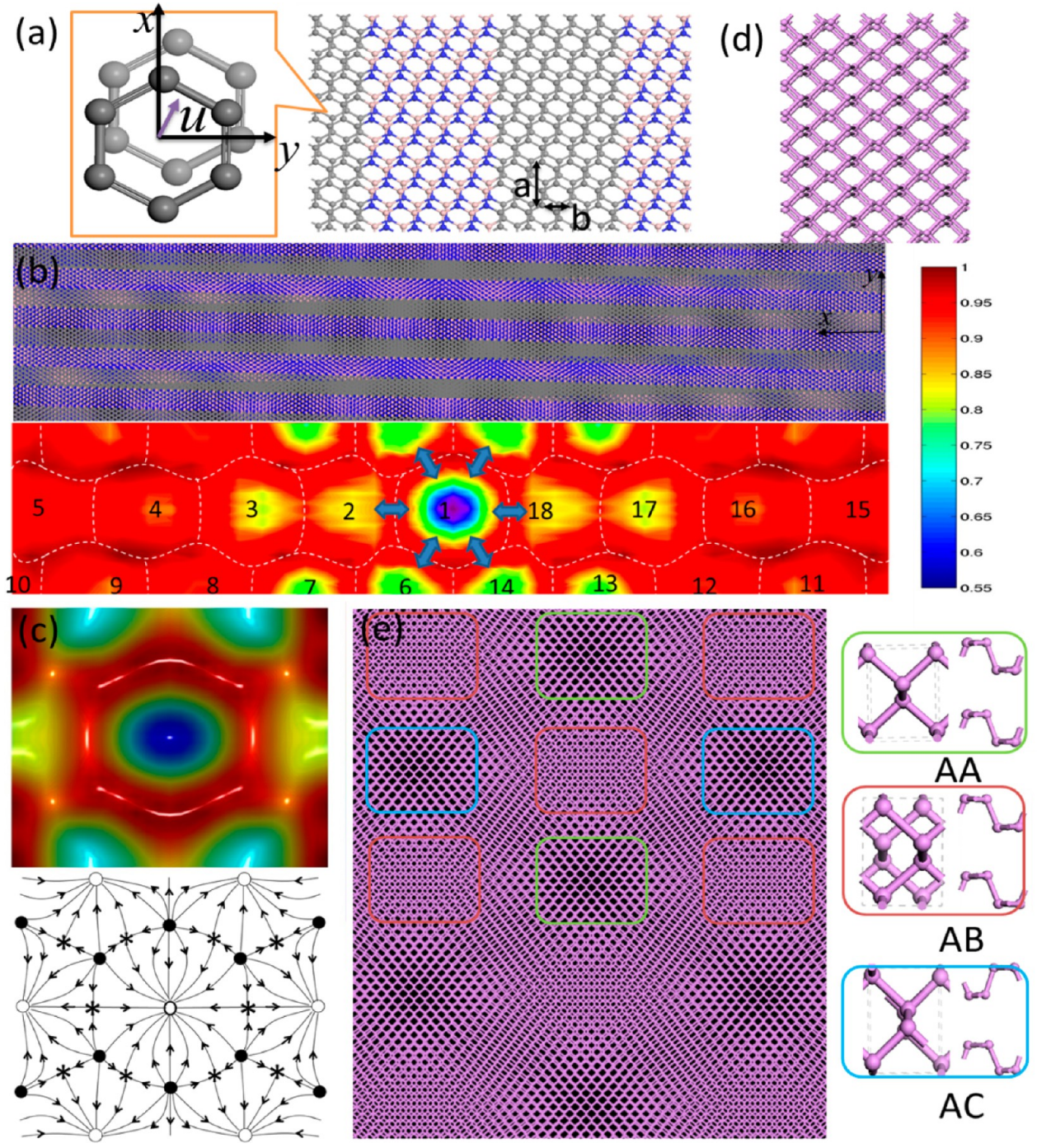

Figure 1. (a) Atomic structure and stack translation $\boldsymbol{u}$ of tbCBN. (b) Moiré pattern of tbCBN with a twist angle of 2.5° and its 3D surface plot of $E_g(\boldsymbol{u}(\boldsymbol{r}))$ in eV for a whole supercell with distinct exciton basins labeled by i = 1−18 and dividing ridges marked by white lines. (c) Exciton basins around i = 1 and streamlines, where open circles, closed circles, and stars denote $E_g(\boldsymbol{r})$ minima (flow attractors), maxima (flow repellers), and saddle points (triple junction of basin watersheds) respectively. (d) Atomic structure of bP and (e) Moiré pattern of tbP with a twist angle of 2.5°. Gray, pink, purple, and blue spheres denote carbon, boron, phosphorus, and nitrogen atoms. AA, AB, and AC stacking regions in (e) are marked by green, red, and blue rectangles.

where $\boldsymbol{g}_j$[12] are the reciprocal vectors, $\boldsymbol{g}_j \cdot \boldsymbol{l}_{j'} \equiv \delta_{jj'}$, and we define $\boldsymbol{u}$ = 0 to be where the generalized stacking fault energy[13] $\gamma(\boldsymbol{u})$ is globally minimized between the two van der Waals (vdW) layers. Usually $\boldsymbol{u}$ = 0 is a high-symmetry stacking arrangement like on-top (AA) or Bernal (AB) stacking. The local atomic environment is completely specified by this translational mismatch $\boldsymbol{u}$, which is gently spatially dependent, and the orientational mismatch θ, which is spatially independent. So local physical properties like the bandgap may be written as $E_g(\boldsymbol{r}) = E_g(\boldsymbol{u}(\boldsymbol{r}),\theta)$ where the first argument is local translational mismatch and the second argument is orientational mismatch of the bilayer. Note that $\boldsymbol{u}(\boldsymbol{r})$ itself depends on θ, so the dependence of $E_g(\boldsymbol{u}(\boldsymbol{r}),\theta)$ on θ comes from both places in the bracket. When θ is really small, we then make the following analytically justified approximation

dx.doi.org/10.1021/nl502414t | Nano Lett. 2014, 14, 5350−5357

$$E_g(\boldsymbol{r}) \approx E_g(\boldsymbol{u}(\boldsymbol{r}), \theta) \approx E_g(\boldsymbol{u}(\boldsymbol{r}), \theta = 0) \quad (1)$$

The last quantity is amenable to density functional theory (DFT) calculations under periodic boundary conditions. In essence, we will perform computations on local bilayer configurations that are perfectly oriented but with varying stack translational mismatch $\boldsymbol{u} \equiv u_x\mathbf{e}_x + u_y\mathbf{e}_y$.

Material Choice of CBN and Black Phosphorus. Carbon/boron nitride (CBN) monolayers with $\{\boldsymbol{l}_j\}$ periodic arrangements of carbon and BN domains have recently been synthesized via photolithography.[14] While the concept and method we present here are general, we decided to use CBN lattices as a model material for the following reasons. While the electronic structure of twisted bilayer graphene is interesting, it is always metallic with zero bandgap. We are interested in $E_g(\boldsymbol{r})$ for exciton funneling and therefore requires semiconducting bilayer. Bilayer MoS_2 would be a good choice but through first-principles calculations we have found its E_g does not change much with $\boldsymbol{u}$. We essentially are trying to design a semiconducting van der Waals (vdW) bilayer with the maximum E_g contrast with respect to $\boldsymbol{u}$ variation. $\boldsymbol{u}$ may be called the (bilayer) slip variable and is akin to the internal shuffling degrees of freedom in crystallography.

CBN is good because it is mechanically and thermally robust with an adjustable in-plane C/BN domain structure or heterolattice.[14] It is a true atomic monolayer sheet, which allows intimate coupling between all atoms of the top layer with all atoms of the bottom layer, unlike in MoS_2 where the cationic layer is more "hidden" and therefore less affected by stack translation. Similar justifications can be made for black phosphorus monolayer[15] or phosphorene. Calculations have already shown large E_g variation in bilayer phosphorene with stacking from E_g = 1.04 eV at AB stacking to E_g = 0.78 eV at AC stacking[16] when no pressure is applied.

We can expect large E_g contrast for twisted bilayer CBN (tbCBN), because the C-rich region, in the limit of large in-plane domain size $l \to \infty$, becomes "metallic" graphene with E_g = 0; whereas the BN-rich region, in the limit of large in-plane domain size $l \to \infty$, becomes "insulating" BN with E_g = 5 eV. With bilayer Moiré superlattice, we therefore expect four limiting stacking environments: "metallic-on-metallic" (MoM), "metallic-on-insulating" (MoI), "insulating-on-metallic" (IoM) and "insulating-on-insulating" (IoI). We will keep using MoM, MoI, IoM, and IoI to label local bilayer stacking environment, even in cases of $l < \Lambda_{MFP}$ where quantum overlap causes the C-rich region to have $E_g > 0$ and BN-rich region to have E_g smaller than 5 eV. With $l \ll \Lambda_{MFP}$ and the alternating ribbon geometry shown next, quantum overlap electronically fuses MoM/IoI regions that are adjacent to each other and MoI/IoM regions that are adjacent and causes the coarse-grained MoM/IoI region with VBM and CBM controlled by MoM (hereon abbreviated as MoM) to have lower band gap than the MoI/IoM regions (hereon abbreviated as IoM). We expect E_g contrast to be tunable by the in-plane domain size or heterolattice spacing $\{\boldsymbol{l}_j\}$ in addition to θ and the interlayer spacing c. Further, if we apply compressive stress normal to the bilayer, c may be reduced and therefore interlayer electronic coupling may be enhanced. Also, if we apply electric field normal to the plane, the self-energies of electronic states on the two layers can be changed. Thus, we expect that normal stress and electric field may also alter E_g contrast in tbCBN and twisted bilayer phosphorene (tbP). These parameters are what we will investigate next by first-principles calculations.

Multiple "Exciton Basins" in Twisted CBN and Phosphorene Bilayer. We study CBN heterolattice with $\boldsymbol{l}_1$ fixed at atomic spacing and $\boldsymbol{l}_2$ varying. As shown in Figure 1a, armchair graphene ribbons and BN ribbons are interlaced with both C and BN ribbon widths n = 9, denoting the number of C−C or B−N dimer along the y-direction. The size of primitive cell along x- and y-direction are defined as $\boldsymbol{l}_1 = a = \sqrt{3}b$ and $\boldsymbol{l}_2 = 9b$, respectively. The internal stacking translation is $\boldsymbol{u} = u_x\mathbf{e}_x + u_y\mathbf{e}_y = (u_x, u_y)$. When one layer is twisted by a small angle θ, the length of the Moiré superlattice will be $L_2 = a/[2\sin(\theta/2)] \approx (a/\theta)$ in y-direction and $L_1 \approx 9b/\theta$ in x-direction. For a clear illustration of the Moiré pattern, we set θ to 2.5° in Figure 1b, so the distance between the two nearest AA stacking domains (arrays of empty holes in Figure 1b) will be around 5.7 nm. At position $\boldsymbol{r} = (r_x, r_y)$, $\boldsymbol{u} \approx (-r_y\theta, r_x\theta)$ modulo $\{\boldsymbol{l}_j\}$, and the 2D bandgap field $E_g(\boldsymbol{u}(\boldsymbol{r}))$ is computed and plotted in Figure 1b,c.

From our calculations, the bandgap map $E_g(\boldsymbol{u}(\boldsymbol{r}))$ is seen to have multiple "drainage basins". $E_g(\boldsymbol{u}(\boldsymbol{r}))$ acts as an effective potential for exciton translational motion, and the bandgap gradient is experimentally demonstrated to control exciton dynamics.[11] This is because the center-of-mass motion of neutral excitons cannot be driven by electric field/band bending, but only by $\nabla E_g(\boldsymbol{u}(\boldsymbol{r}))$. The neutral excitons should therefore be funneled to local E_g minima, $\boldsymbol{r}_i^{\min} \equiv \arg\min E_g(\boldsymbol{u}(\boldsymbol{r}))$, where i labels the drainage basin, a contiguous region of $\boldsymbol{r}$ where exciton created are expected to flow to $\boldsymbol{r}_i^{\min}$ in downhill dynamics, and arg min stands for the argument of the minimum, the set of points of the given argument for which E_g attains local minima. From our calculations, we find i runs from 1 to 18. In other words, there exists I = 18 distinct exciton drainage basins within one twisted bilayer CBN supercell. Even if we exclude those basins related by point-group symmetry, there are still I' = 10 unique basins with different min E_g and shape/size. Between two adjacent basins i and i', there will be one or more saddle points $\boldsymbol{r}_{ii'}^{\text{saddle}}(s)$. The watershed, or dividing ridge $\boldsymbol{r}_{ii'}^{\text{watershed}}(s)$, that separates two nearby basins are marked as white lines in Figure 1b. It can be computed by integrating the streamline equation

$$\frac{d\boldsymbol{r}}{ds} = -\nabla E_g(\boldsymbol{r}(s)) \quad (1)$$

that goes through the saddle point (s is a scalar streamline length parameter). Three dividing ridges $\boldsymbol{r}_{ii'}^{\text{watershed}}(s)$, $\boldsymbol{r}_{ii''}^{\text{watershed}}(s)$, $\boldsymbol{r}_{i'i''}^{\text{watershed}}(s)$ meet at a triple junction point $\boldsymbol{r}_{ii'i''}^{\text{triple}}$, which has to be a local maxima in E_g. A detailed view of exciton basins around i = 1 and streamline pattern is plotted in Figure 1c. The streamlines are computed based on (1), with $\boldsymbol{r}_i^{\min}$ funnel centers as the flow attractors, $\boldsymbol{r}_{ii'i''}^{\text{triple}}$ as flow repellers, and dividing ridges $\{\boldsymbol{r}_{ii'}^{\text{watershed}}(s)\}$ that set the boundaries of each basin.

Such intricate patterns of exciton drainage basins (Figure 1b,c) are surprising for a simple twisted structure. By atomic structure design, for example, tuning the shape of the periodic C and BN domains,[14] we may further engineer the energy-flow pattern. We also note here that when θ is tiny but varying, the $E_g(\boldsymbol{u}(\boldsymbol{r}))$ maps thus created are self-similar with peak and valley E_g values invariant, but just spatially scaling as $1/\theta$. But when θ gets large, we will enter into quantum interference regime and a new set of quantum-coherent behaviors may emerge. The opportunity presented here for exciton engineering with twisted vdW bilayer is quite dramatic and a step toward the sophistication of biological light-harvesting complexes such as photosynthetic systems.

dx.doi.org/10.1021/nl502414t | Nano Lett. 2014, 14, 5350−5357

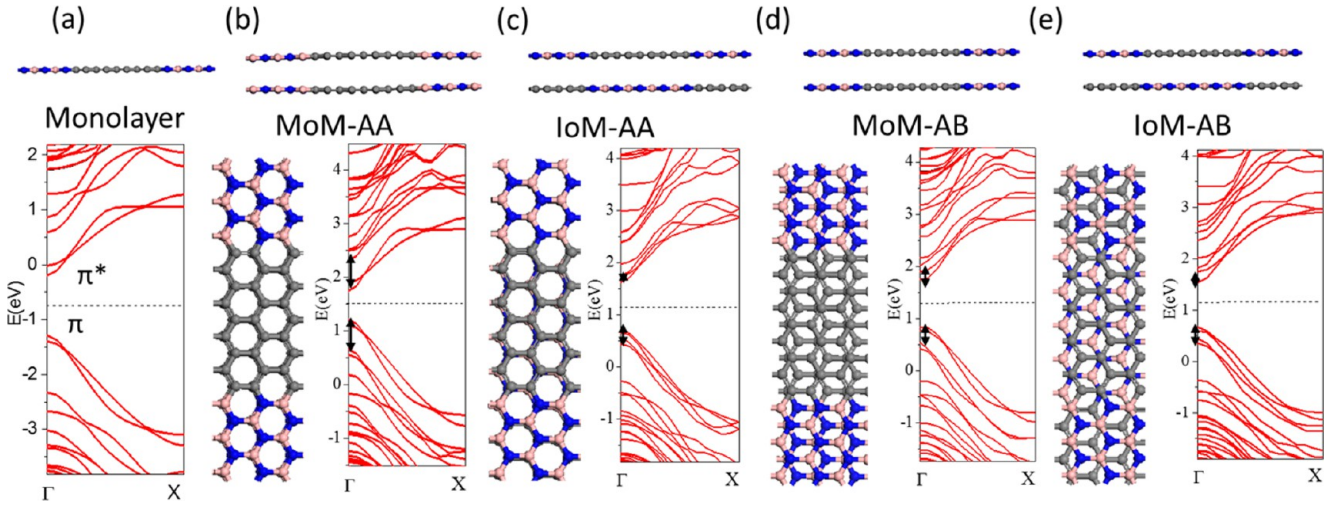

Figure 2. Geometric and band structures of (a) CBN monolayer and CBN bilayer (both side view and plan view) with stacking style (b) MoM-AA, (c) IoM-AA, (d) MoM-AB, and (e) IoM-AB. Among them the IoM-AB structure in (e) is the ground state, while the structures in panels b–d are only 0.0103, 0.0062, and 0.0004 eV/atom higher in energy. π–π band splittings are marked by black arrows.

$E_g(\boldsymbol{u}(\boldsymbol{r}))$ of tbCBN ranges from 0.53 to 1.06 eV and achieves local minima close to AA stacking domains, leading to a triangular array of exciton basins. However, those local minimum values at AA regions are also different, ranging from 0.53 to 0.95 eV, and the lowest value 0.53 eV is located at where bilayer graphene–graphene domains are completely overlapping (MoM). The funnel center of this globally lowest i = 1 basin, $E_g(\boldsymbol{u}(\boldsymbol{r}_1^{\min}))$ = 0.53 eV, has MoM-AA stacking locally, where MoM (vs IoM) is called major label, while AA (vs AB, AC, etc.) is called the minor label, of the stacking configuration. The major label here controls the exciton basin index i, while the minor label defines the funnel center of each basin.

In comparison, the bandgap landscape of tbP is much simpler. As shown in Figure 1e, the Moiré supercell is rectangular and consists of prototypical AA, AB, and AC stacking regions (in yellow, blue, and red rectangles, respectively). According to previous calculations,[16] their local E_g are 0.95, 1.04, and 0.78 eV, and there are only I' = 2 types of unique exciton funnels, unrelated by symmetry, with funnel centers labeled by AA and AC stacking with $E_g(\boldsymbol{u}(\boldsymbol{r}_1^{\min}))$ = 0.95 eV and $E_g(\boldsymbol{u}(\boldsymbol{r}_2^{\min}))$ = 0.78 eV, respectively, surrounded by regions with locally maximal E_g = 1.04 eV at AB stacking.

Electronic Structure Details of the In-Plane Crystal but Out-of-Plane Molecule. To illustrate the material and structure sensitivities, here we performed detailed investigations of tbCBN with multiple exciton basins. Figure 2 displays the geometric and band structures of some representative stacking environments with $\boldsymbol{u}$ either AA or AB (the minor label), while the graphene domains of one layer may be stacked on either graphene domains (Figure 2b,d, MoM) or BN domains of the other layer (Figure 2c,e, IoM), and those four configurations in Figure 2b–e are labeled as MoM-AA (0,0), IoM-AA (a/3, 9b/2), MoM-AB (a/3, 0) and IoM-AB (a/3, 9b/2). Their band gaps in Figure 2b–e are 0.53, 0.88, 0.91, and 0.86 eV compared with 1.09 eV of the n = 9 base monolayer.

There are four bands near the Fermi level in the monolayer CBN bandstructure, denoted as the lowest unoccupied electron states (LUES), second LUES (SLUES), the highest occupied electron state (HOES), and second HOES (SHOES), which are all distributed in graphene domains and identified as π and π^* orbitals (see Supporting Information Figure S1). As we compare the bandstructures of CBN bilayer in Figure 2b–e with monolayer in Figure 2a, we find that their HOES, SHOES, LUES, SLUES are all split into 8 bands. This resembles the splitting of two hybridized electronic orbitals in a molecule but for tbCBN this hybridization takes place between two bands of periodic monolayer systems. The splitting is due to the overlap integral of π-orbitals on two layers including the contribution from the electron–electron interactions,[17] which leads to the splitting of HOES and LUES, shifting HOES and LUES closer to each other and reducing E_g. For MoM-AA stacking, the π-orbitals of graphene domains of bilayer are maximally superposed, which result in high interaction, while the staggering of π-clouds of the other three stacking styles greatly reduces the π–π interlayer interaction and the splitting of HOES and LUES. This can be verified by the splitting strength of HOES δ in Figure 2b–e, which are 0.56, 0.17, 0.29, and 0.23 eV, respectively.

E_g as $\boldsymbol{u}$ changes from (0, 0) = AA to (a, 0) = AA and from (0, 0) = AA to (0, 9b) = AA is plotted in Figure 3a,b, respectively, corresponding to the lines r_x = 0, 0 < r_y <L_2 and r_y = 0, 0 <r_x <L_1 in Figure 1b. We define the area of a carbon hexagonal ring in graphene domain as S_0, and the overlapping area of two hexagonal carbon rings in bilayer as S (see details in Supporting Information Figure S3). We plot the change of S from (0, 0) to (a, 0) and from (0, 0) to (0, b) in Supporting Information Figure S3. The minimum-S stacking is located at $\boldsymbol{u}$ = (a/3, 0), (2a/3, 0) and (0, b/2) where E_g is the largest, and E_g will decrease when S increases as larger π overlapping leads to stronger interlayer interaction as well as HOES splitting strength δ.

The curve of E_g variation from (0, 0) to (0, 9b) is symmetrical about u_y = 4.5b and exhibits an oscillating behavior. For those exciton basin centers labeled i = 1–5 at AA stacking (black circles), E_g(0, 0) = 0.53 eV, E_g(0, b) = 0.81 eV, E_g(0, 2b) =0.78 eV, E_g(0, 3b)=0.81 eV, E_g(0, 4b)=0.95 eV, with HOES splitting δ = 0.56, 0.32, 0.34, 0.26, and 0.13 eV respectively. As a general trend, they match our expectation that E_g should increase as the splitting δ decreases with the narrowing bigraphene domain (MoM region) width m. However, why is E_g(0, 0) much smaller than E_g(0, b), while E_g(0,b) is nearly the same as, and even 0.03 eV larger than E_g(0, 2b)? Here δ is seen

dx.doi.org/10.1021/nl502414t | Nano Lett. 2014, 14, 5350–5357

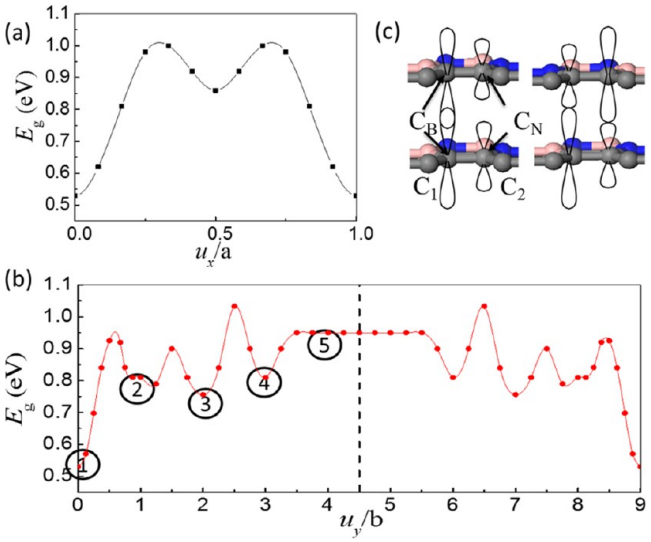

Figure 3. (a) $E_g(\boldsymbol{u})$ along (0, 0) to (a, 0); (b) $E_g(\boldsymbol{u})$ from (0, 0) to (0, 9b). (c) Illustration of edge carbon $\pi-\pi$ overlapping in MoM-AA stacking.

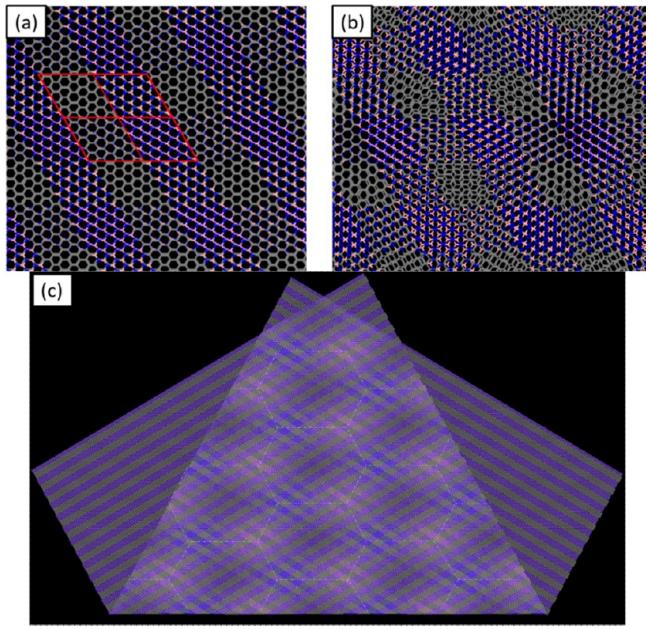

Figure 4. Moiré patterns of CBN bilayer with a twist of (a) 60° and (b) 62.5° on the top layer, respectively. (c) CBN monolayer folding at an angle of 60.25°.

to be not linear with respect to the bigraphene domain width m, and we attribute δ-u_y saturation to an edge effect: on the edge of the bigraphene domain, the charge carried by carbon atoms C_B, C_N, C_1, and C_2 (illustrated in Figure 3c) are $-0.086e$, $0.058e$, $0.006e$, and $-0.011e$ according to Hirshfeld analysis.[18] For the carbon atom C_B bonded to a boron atom in MoM-AA environment, the considerable π-electron transferring from B atom (see charge density in Supporting Information Figure S1) will lead to much stronger $\pi-\pi$ overlapping with the C_B atom above it. As shown in Figure 3c, if we twist the upper layer 180° so a C_N atom is above the C_B atom, the bandgap will increase from 0.53 to 0.66 eV while δ will decrease from 0.56 to 0.42 eV. This shows that a considerable portion of $\pi-\pi$ overlapping concentrates on the graphene edges. This is also verified in the discussion in Supporting Information (Figure S4). The postsaturation small oscillations in δ-u_y may be attributable to quantum confinement. The MoM width at (0, b) and (0, 2b) are m = 7 and 5; for reference, CBN monolayer with n = 7 and 5 has bandgap 0.90 and 0.84 eV, respectively, which may explain why $E_g(0, b)$ is larger than $E_g(0, 2b)$.

Vicinal Twisted Bilayer. A large Moiré superlattice $\{\boldsymbol{L}_i\}$ with $L_i \gg \lambda_{photon}$, Λ_{MFP} may also be generated when θ is very close to a large but special angle like 60°. In the theory of grain boundaries, these are called vicinal boundaries, which differ in misorientation from so-called special grain boundary by a small amount. Vicinal grain boundary can be quite like small-angle grain boundary. Indeed, the Moiré patterns of graphene bilayer at a small twisting angle θ and at an angle of 60° + θ are identical. However, tbCBN vicinal to 60° is distinct from small-θ tbCBN due to lack of three-fold symmetry. At a twisting angle 60°, tbCBN will have a rhombic supercell with side length 6a. As shown by the red lines in Figure 4a, it is evenly divided into four regions: graphene−graphene overlapping (MoM), BN−BN overlapping (IoI), and two graphene−BN overlapping (IoM and MoI). This metamaterial resembles binary nanoparticle superlattice of semiconductor quantum dots[19,20] composed of different bandgap domains. On the basis of this structure, when the twisting angle increases to $\theta = 60° + \phi$ as shown in Figure 4b, a Moiré pattern will be superimposed on this 2D CBN superlattice with $6a/\phi$ as the side length of its rhombic unit cell. There will be only one type of exciton basin located at AA, unlike the multiple exciton basins for small-θ tbCBN. It is interesting to take notice of the three levels of periodicity within the vicinal tbCBN here: the hexagonal atomic rings (primitive structure), the 6a rhombic MoM, IoI, IoM/MoI binary nanoparticle superlattice at θ = 60° (secondary structure), and the $6a/\phi$ Moiré superlattice pattern at $\theta = 60° + \phi$ (tertiary structure). All three levels of structures impact $E_g(\boldsymbol{u}(\boldsymbol{r}))$, although it is the tertiary structure that sets the exciton basin size here.

In ref 1, the maximum effective exciton funnel radius, which is equal to the exciton drift length before radiative recombination, was estimated to be around 660−3000 nm. If we suppose the Moiré superlattice period L is approximately of the same magnitude, the twist angle θ should be around 0.05−0.22° or 60 ± 0.05−0.22°. Note that the twisting angle has been measured to be as low as 0.1° experimentally,[21] although such a minute angle was not intentionally controlled. To achieve bilayer Moiré superlattice, one may simply mechanically fold a monolayer at some angle. To visualize it clearly, we fold a CBN monolayer at an angle of 60.25° so the angle of between the ribbon directions of two layers is 59.50° and the periodicity of Moiré superlattice will be around 300 nm. Then the Moiré tertiary pattern can be visualized by the empty-hole arrays in Figure 4c with dividing ridges of the exciton basins outlined in white.

Further Enhancement of Bandgap Contrast. The Young's modulus of graphite is around 1TPa in-plane but only 15 GPa out-of-plane, so it is relatively easy to change the interlayer distance c by out-of-plane pressure. With such vertical elastic strain engineering (ESE)[22] of CBN bilayer, the increasing interlayer interaction can cause larger splitting of LUES−SLUES and HOES−SHOES and further reduce the bandgap. This assumption can be verified by the dependence of E_g on the interlayer distance in Figure 5a. Again different stacking $\boldsymbol{u}$ will play a decisive role: for MoM-AA, E_g will decline much faster with the bilayer compression and will drop to only

dx.doi.org/10.1021/nl502414t | Nano Lett. 2014, 14, 5350−5357

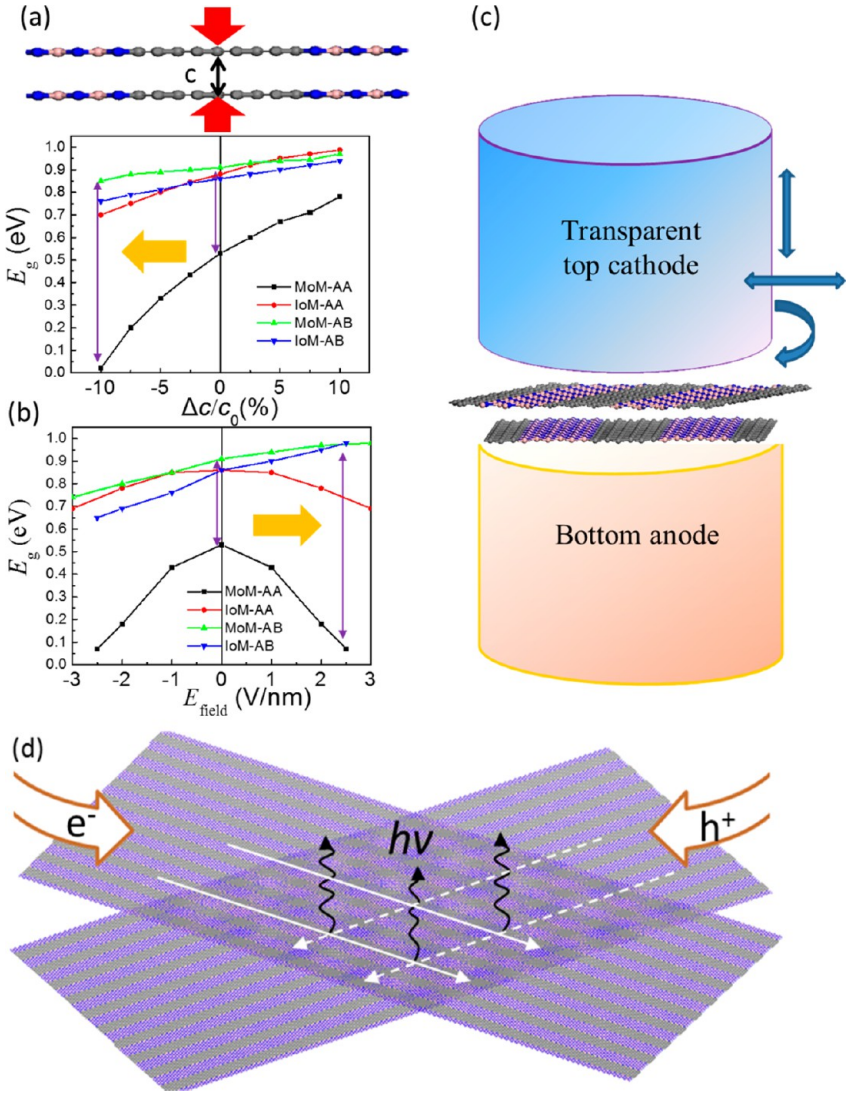

Figure 5. (a) Illustration of a tbCBN with a pressure applied in the vertical direction, and the dependence of E_g on the change of interlayer distance Δc for four different stacking styles. (b) Dependence of E_g on the external electric field in the vertical direction. The bandgap contrast is doubled at $\Delta c = -0.1c_0$ or $E_{field} = 0.25$ V/nm as shown by purple arrows. Schematic of (c) a band gap tuning device and (d) its application as light emitter.

0.02 eV when the interlayer distance is 10% shorter, becoming almost metallic. Thus, a local semiconductor-to-metal transition is predicted for tbCBN if a moderate normal pressure is applied. For the other three stacking ***u***'s IoM-AA, MoM-AB, and IoM-AB, their band gaps only change slightly to 0.70, 0.86, and 0.76 eV, respectively. Therefore, we can obtain a much wider bandgap contrast varying from metallic to 0.86 eV by Moiré superlattice, more than doubled in comparison with the range [0.53, 0.91]eV without pressure. The pressure required for interlayer distance to be compressed by 10% is 7.5 GPa for MoM-AA, which is much smaller than for other three stacking styles.

We find that a larger E_g contrast can also be achieved by applying an external electric field in the vertical direction, as shown in Figure 5b: for MoM-AA stacking E_g will decrease drastically with increasing magnitude of electric field in either direction, which is much more sensitive compared with other three stacking styles. Moreover, for MoM-AB and IoM-AB stacking, E_g can even be enhanced by electric field. Therefore, at an electric field of 2.5 V/nm, the E_g contrast of Moiré superlattice will be [0.07, 0.98] eV.

In Figure 5c, we propose a design of engineering the E_g contrast of Moiré superlattice: one CBN monolayer is attached to the bottom anode and another is attached to the top cathode, where the cathode can be mechanically rotated and can translate in-plane or vertically. Therefore, it can easily control θ and interlayer distance so as to tune the range of varying band gap. The cathode needs to be transparent and conducting so as not to block the incoming light when the device is used for photovoltaic conversion, and two semiconducting buffer layers may be placed between tbCBN and the two electrodes, which serve as electron-selective and hole-selective transporters. Electric field may also be applied in the vertical direction to further broaden the range of spectrum. This Moiré superlattice may be used as a tunable light emitter if charge is injected from electrical contacts at different locations with a much broader spectrum than pure BN that has already been used as an ultraviolet light emitter. As shown in Figure 5d, if we inject electrons to upper layer and holes to lower layer, they will combine with each other at junctions of graphene overlapping regions as flowing along the direction of graphene

dx.doi.org/10.1021/nl502414t | *Nano Lett.* 2014, 14, 5350−5357

ribbons, giving rise to the emission of light with distinct colors from different exciton funnels.

Discussion. So far we have assumed we can impose a rigid-rotational slip displacement $\boldsymbol{u}_0 = \mathbf{R}\,\boldsymbol{r} - \boldsymbol{r}$, that generates no in-plane strain or out-of-plane waviness. $\mathbf{R}$ is a rotational matrix, $\mathbf{R}^T\mathbf{R} = \mathbf{I}$. However, a question remains whether there will be additional relaxational displacement on top of the imposed rotational displacement: $\boldsymbol{u} = \mathbf{R}\,\boldsymbol{r} + \boldsymbol{u}_{\mathrm{relax}}(\boldsymbol{r})$, for a free-standing bilayer. The precise answer is that generally (a) $\boldsymbol{u}_{\mathrm{relax}}(\boldsymbol{r})$ will exist, and it will be a periodic function with the same period as the Moiré superlattice; and (b) its amplitude will be very small though. The reason for (a) is that the unrelaxed slip displacement $\boldsymbol{u}_0 = \mathbf{R}\,\boldsymbol{r} - \boldsymbol{r}$ will induce a layer-to-layer traction density $\mathbf{t}(\boldsymbol{r}) \equiv -\partial\gamma(\boldsymbol{u})/\partial\boldsymbol{u}$, where $\gamma(\boldsymbol{u})$ is the bilayer generalized stacking fault energy.[13,23] This layer-to-layer traction density is spatially dependent, just like the band gap, and generally it will have a finite divergence: $\nabla\cdot\,\mathbf{t}(\boldsymbol{r}) \neq 0$, which means in a free-body diagram analysis of the upper layer, the bottom layer would exert to it an inhomogeneous traction density that causes nonzero net force locally. This would in turn drive an additional relaxational displacement $\boldsymbol{u}_{\mathrm{relax}}(\boldsymbol{r})$ that can have both in-plane and out-of-plane components. The in-plane component of $\boldsymbol{u}_{\mathrm{relax}}(\boldsymbol{r})$ can cause in-plane strain, and the out-of-plane component can cause waviness. So a truly free-standing twisted bilayer would generally have some in-plane strain and out-of-plane waviness, due to this relaxational displacement $\boldsymbol{u}_{\mathrm{relax}}(\boldsymbol{r})$.

However, the in-plane relaxational displacement should be very small compared to the imposed slip $\boldsymbol{u}_0 = \mathbf{R}\,\boldsymbol{r} - \boldsymbol{r}$. This is because the layer-to-layer traction due to van der Waals interaction is very weak and needs to work against the in-plane Young's modulus (E) to generate the relaxational displacement. E is due to the in-plane primary bonds and is very large (~1 TPa for CBN in-plane). Therefore, $\boldsymbol{u}_{\mathrm{relax}}(\boldsymbol{r}) \ll \boldsymbol{u}_0$. We can see this in the limit of large layer-to-layer separation $c \to \infty$ and van der Waals traction $\to 0$, where one can clearly impose rigid-body rotation with $\boldsymbol{u}_{\mathrm{relax}}(\boldsymbol{r}) = 0$. So, in this paper we have neglected the effect of $\boldsymbol{u}_{\mathrm{relax}}(\boldsymbol{r})$. The out-of-plane waviness generally gives smaller, higher-order correction to the electronic structure, compared to in-plane slip or strain. Such waviness may also be suppressed by an overall tension, which is needed even for "free-standing" graphene. Lastly, we note that since $\boldsymbol{u}_{\mathrm{relax}}(\boldsymbol{r})$ has the same periodicity as the Moiré superlattice, its effect will be to conformally distort the $E_g(\boldsymbol{r}) \to E_g(\boldsymbol{r}')$ pattern but will not change the peak and valley heights, periodicity, flow basin topologies, and so forth. So all the qualitative points made in the paper are robust.

Outlook. Our twisted van der Waals bilayer may be regarded as an in-plane crystal but an out-of-plane molecule. Its interaction with light can be tuned by the secondary (in the case of small θ) and even tertiary (in the case of vicinal θ) periodic structures in-plane and by applying pressure and electric field out-of-plane. The multiple exciton basins and the rich chemistry and physics brought by such a simple twist mimics the complexity of biological light-harvesting systems. Even though not shown, this principle can also work with CBN multilayer, h-BN bilayer embedded with graphene quantum dots, and even pure h-BN bilayer, and we expect that this design may be applied to many other atomically thin layers, including GaS, GaSe, GaTe, MX_2-type dichalcogenides, graphitic carbon nitride, and so on. A solar cell or light emitter with easily controllable bandgap contrast may be built. CBN monolayer has already been used as a split closed-loop resonator that works as a bandpass filter for high-frequency application,[12,14] and the tunability of Moiré patterns may turn out to be advantageous.

Methods. Density functional theory (DFT) calculations are performed by using the Vienna ab initio simulation package (VASP).[24,25] We have employed projector augmented-wave (PAW)[26] method, Perdew–Burke–Ernzerhof (PBE) of exchange-correlation functional, an energy cutoff of 400 eV for the plane-wave basis and Monkhorst–Pack $\mathbf{k}$-point sampling of $10 \times 3 \times 1$. Geometry optimizations were performed with a criterion of the maximum residual force less than 0.02 eV/Å. A semiempirical correction using Grimme method (D2)[27] was also applied to take the van der Waals interaction into account. The curves of E_g varying with $\boldsymbol{r}$ or $\boldsymbol{u}$ were obtained upon constant interlayer distance at MoM-AA stacking.

It is known that DFT with PBE can underestimate the band gaps of materials, although here the general trends of stacking style dependent and interlayer distance dependent band gap of CBN bilayer are unlikely to change. We re-examined the band gap of bilayer using the screened exchange hybrid Heyd–Scuseria–Ernzerhof (HSE)[28] functional. However, every unit cell of bilayer in Figure 2b–e contains 72 atoms, and it will be very time-consuming to compute by using HSE. As a result, we select CBN bilayer with both graphene and BN domain width $n = 4$, which is much narrower, as shown in Supporting Information Figure S5. The calculated band gap of MoM-AA and IoM-AB stacking are respectively 0.85, 1.15 eV by using PBE, and 1.35, 1.58 eV by using HSE; after the interlayer distance is compressed by 10%, the calculated band gap of MoM-AA and IoM-AB stacking decline to respectively 0.35, 0.95 eV by using PBE, and 0.80, 1.45 eV by using HSE. It seems that the difference between PBE and HSE results is constantly around 0.5 eV, while the dependence of band gap on stacking style and interlayer distance remains. Therefore, in Figure 4a for HSE results it will be likely that the band gap range is around [1.03, 1.41]eV at zero pressure, and [0.52, 1.36]eV at $\Delta c = -0.1c_0$. To obtain its accurate optical absorption spectrum, the GW[29,30]–Bethe–Salpeter–equation[31,32] (GW-BSE) method is required, which is still very time-consuming for this system. However, we find that pure h-BN bilayer can also exhibit similar behavior when changing the stacking style or interlayer distance. To our PBE results, the band gap of h-BN bilayer is 4.57 eV for AB stacking but only 3.99 eV for AA stacking; it even declines to 3.49 eV as the interlayer distance is compressed by 10%. In Supporting Information Figure S5e, we plot their optical adsorption spectrum by using GW-BSE method: the first peak moves from 5.31 eV of AB stacking to 5.21 eV of AA stacking, and then to 5.10 eV when compressed by 10%, which accords with the trend of band gap change.

■ ASSOCIATED CONTENT

Ⓢ Supporting Information

HOES, SHOES, LUES, SLUES, electron density, and deformation density distributions of CBN monolayer and bilayer, $S(\boldsymbol{u})$ and estimated $E_g(S(\boldsymbol{u}))$, configurations of CBN bilayer with graphene domain width $n = 5$ on upper layer and $n = 9$ on lower layer, bandstructures calculated by using PBE and HSE, and optical adsorption spectrum of BN bilayer. This material is available free of charge via the Internet at http://pubs.acs.org.

■ AUTHOR INFORMATION

Corresponding Author

*E-mail: liju@mit.edu.

Notes

The authors declare no competing financial interest.

■ ACKNOWLEDGMENTS

We acknowledges support by NSF DMR-1120901. Computational time on the Extreme Science and Engineering Discovery Environment (XSEDE) under Grants TG-DMR130038, TG-DMR140003, and TG-PHY140014 is gratefully acknowledged.

■ REFERENCES

(1) Feng, J.; Qian, X.; Huang, C.-W.; Li, J. *Nat. Photonics* **2012**, *6*, 866−872.
(2) Suess, M. J.; Geiger, R.; Minamisawa, R. A.; Schiefler, G.; Frigerio, J.; Chrastina, D.; Isella, G.; Spolenak, R.; Faist, J.; Sigg, H. *Nat. Photonics* **2013**, *7*, 466−472.
(3) Nam, D.; Sukhdeo, D. S.; Kang, J.-H.; Petykiewicz, J.; Lee, J. H.; Jung, W. S.; Vučković, J.; Brongersma, M. L.; Saraswat, K. C. *Nano Lett.* **2013**, *13*, 3118−3123.
(4) Yankowitz, M.; Xue, J.; Cormode, D.; Sanchez-Yamagishi, J. D.; Watanabe, K.; Taniguchi, T.; Jarillo-Herrero, P.; Jacquod, P.; LeRoy, B. J. *Nat. Phys.* **2012**, *8*, 382−386.
(5) Lopes dos Santos, J. M. B.; Peres, N. M. R.; Castro Neto, A. H. *Phys. Rev. Lett.* **2007**, *99*, 256802.
(6) Kim, K.; Coh, S.; Tan, L. Z.; Regan, W.; Yuk, J. M.; Chatterjee, E.; Crommie, M. F.; Cohen, M. L.; Louie, S. G.; Zettl, A. *Phys. Rev. Lett.* **2012**, *108*, 246103.
(7) Ponomarenko, L. A.; Gorbachev, R. V.; Yu, G. L.; Elias, D. C.; Jalil, R.; Patel, A. A.; Mishchenko, A.; Mayorov, A. S.; Woods, C. R.; Wallbank, J. R.; Mucha-Kruczynski, M.; Piot, B. A.; Potemski, M.; Grigorieva, I. V.; Novoselov, K. S.; Guinea, F.; Fal'ko, V. I.; Geim, A. K. *Nature* **2013**, *497*, 594−597.
(8) Dean, C. R.; Wang, L.; Maher, P.; Forsythe, C.; Ghahari, F.; Gao, Y.; Katoch, J.; Ishigami, M.; Moon, P.; Koshino, M.; Taniguchi, T.; Watanabe, K.; Shepard, K. L.; Hone, J.; Kim, P. *Nature* **2013**, *497*, 598−602.
(9) Hunt, B.; Sanchez-Yamagishi, J. D.; Young, A. F.; Yankowitz, M.; LeRoy, B. J.; Watanabe, K.; Taniguchi, T.; Moon, P.; Koshino, M.; Jarillo-Herrero, P.; Ashoori, R. C. *Science* **2013**, *340*, 1427−1430.
(10) Shockley, W.; Queisser, H. J. *J. Appl. Phys.* **1961**, *32*, 510−519.
(11) Fu, X.; Su, C.; Fu, Q.; Zhu, X.; Zhu, R.; Liu, C.; Liao, Z.; Xu, J.; Guo, W.; Feng, J.; Li, J.; Yu, D. *Adv. Mater.* **2014**, *26*, 2572−2579.
(12) Ci, L.; Song, L.; Jin, C.; Jariwala, D.; Wu, D.; Li, Y.; Srivastava, A.; Wang, Z. F.; Storr, K.; Balicas, L.; Liu, F.; Ajayan, P. M. *Nat. Mater.* **2010**, *9*, 430−435.
(13) Qi, L.; Mao, Y. W.; Li, J. *Nanoscale* **2012**, *4*, 5989−5997.
(14) Liu, Z.; Ma, L.; Shi, G.; Zhou, W.; Gong, Y.; Lei, S.; Yang, X.; Zhang, J.; Yu, J.; Hackenberg, K. P.; Babakhani, A.; Idrobo, J. C.; Vajtai, R.; Lou, J.; Ajayan, P. M. *Nat. Nanotechnol.* **2013**, *8*, 119−24.
(15) Li, L.; Yu, Y.; Ye, G. J.; Ge, Q.; Ou, X.; Wu, H.; Feng, D.; Chen, X. H.; Zhang, Y. *Nat. Nano.* **2014**, *9*, 372−377.
(16) Dai, J.; Zeng, X. C. *J. Phys. Chem. Lett.* **2014**, *5*, 1289−1293.
(17) Berashevich, J.; Chakraborty, T. *J. Phys. Chem. C* **2011**, *115*, 24666−24673.
(18) Hirshfeld, F. L. *Theor. Chim. Acta* **1977**, *44*, 129−138.
(19) Shevchenko, E. V.; Talapin, D. V.; Kotov, N. A.; O'Brien, S.; Murray, C. B. *Nature* **2006**, *439*, 55−59.
(20) Ye, X.; Chen, J.; Engel, M.; Millan, J. A.; Li, W.; Qi, L.; Xing, G.; Collins, J. E.; Kagan, C. R.; Li, J.; Glotzer, S. C.; Murray, C. B. *Nat. Chem.* **2013**, *5*, 466−473.
(21) Kim, K. S.; Walter, A. L.; Moreschini, L.; Seyller, T.; Horn, K.; Rotenberg, E.; Bostwick, A. *Nat. Mater.* **2013**, *12*, 887−892.
(22) Li, J.; Shan, Z.; Ma, E. *MRS Bull.* **2014**, *39*, 108−114.
(23) Shen, C.; Li, J.; Wang, Y. *Acta Mater.* **2014**, *74*, 125−131.
(24) Kresse, G.; Furthmüller, J. *Phys. Rev. B* **1996**, *54*, 11169−11186.
(25) Kresse, G.; Furthmüller, J. *Comput. Mater. Sci.* **1996**, *6*, 15−50.
(26) Blöchl, P. E. *Phys. Rev. B* **1994**, *50*, 17953−17979.
(27) Grimme, S. *J. Comput. Chem.* **2006**, *27*, 1787−1799.
(28) Heyd, J.; Scuseria, G. E.; Ernzerhof, M. *J. Chem. Phys.* **2003**, *118*, 8207−8215.
(29) Hedin, L. *Phys. Rev.* **1965**, *139*, A796−A823.
(30) Hybertsen, M. S.; Louie, S. G. *Phys. Rev. Lett.* **1985**, *55*, 1418−1421.
(31) Salpeter, E. E.; Bethe, H. A. *Phys. Rev.* **1951**, *84*, 1232−1242.
(32) Onida, G.; Reining, L.; Rubio, A. *Rev. Mod. Phys.* **2002**, *74*, 601−659.

Supporting Information

Tunable exciton funnel using Moiré superlattice in twisted van der Waals bilayer

Menghao Wu, Xiaofeng Qian and Ju Li*
Department of Nuclear Science and Engineering and Department of Materials Science and Engineering, Massachusetts Institute of Technology, Cambridge, Massachusetts 02139, USA
* To whom correspondence should be addressed: liju@mit.edu

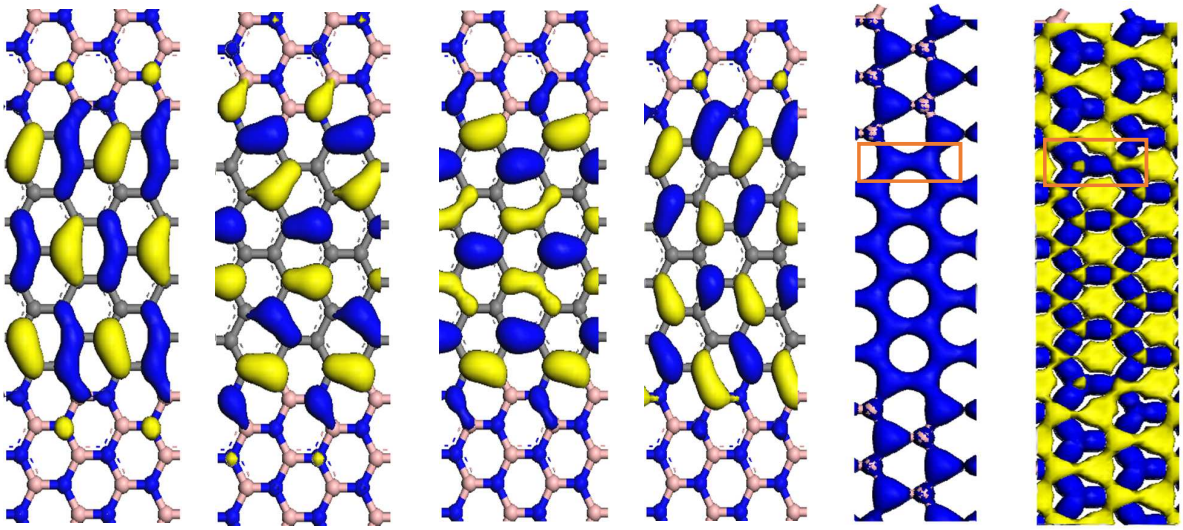

Figure S1 HOES, SHOES, LUES, SLUES, electron density and deformation density distributions of CBN monolayer. We use a red rectangle to mark a C_B and a C_N atom which exhibit similar behavior as a N and B atom in BN domain respectively.

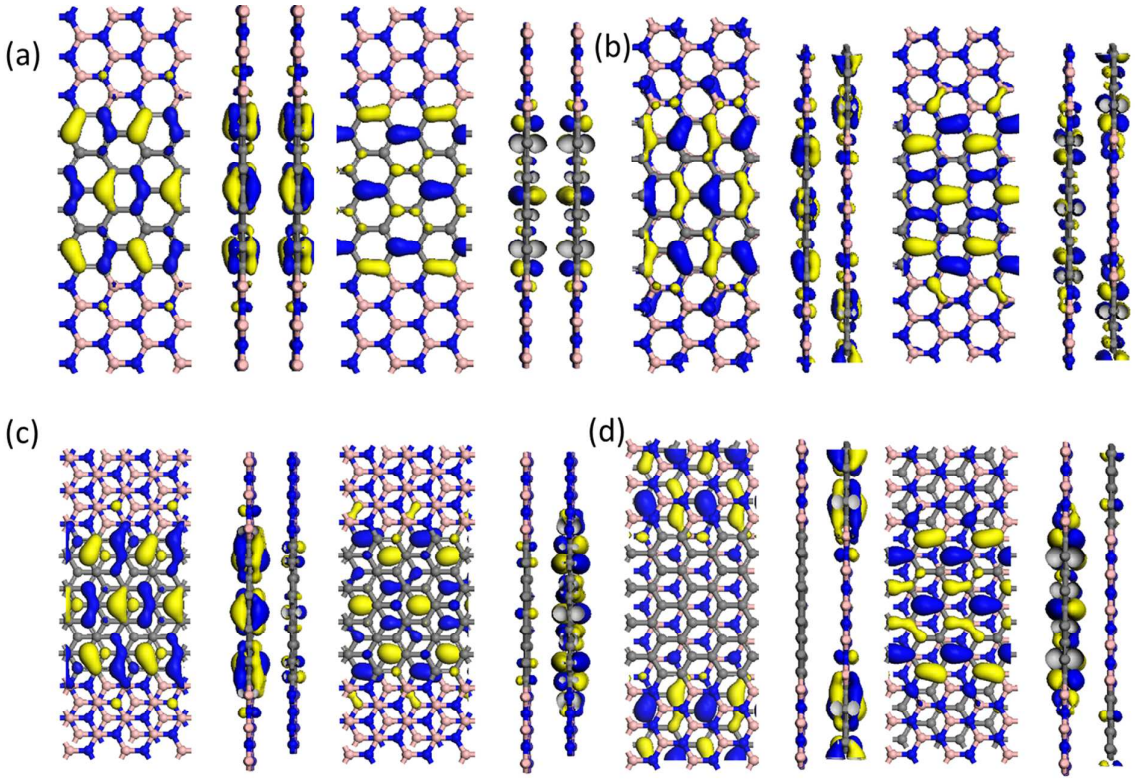

Figure S2 HOES and LUES distributions of CBN bilayer with stacking style (a)MoM-AA, (b)IoM-AA, (c)MoM-AB and (d)IoM-AB.

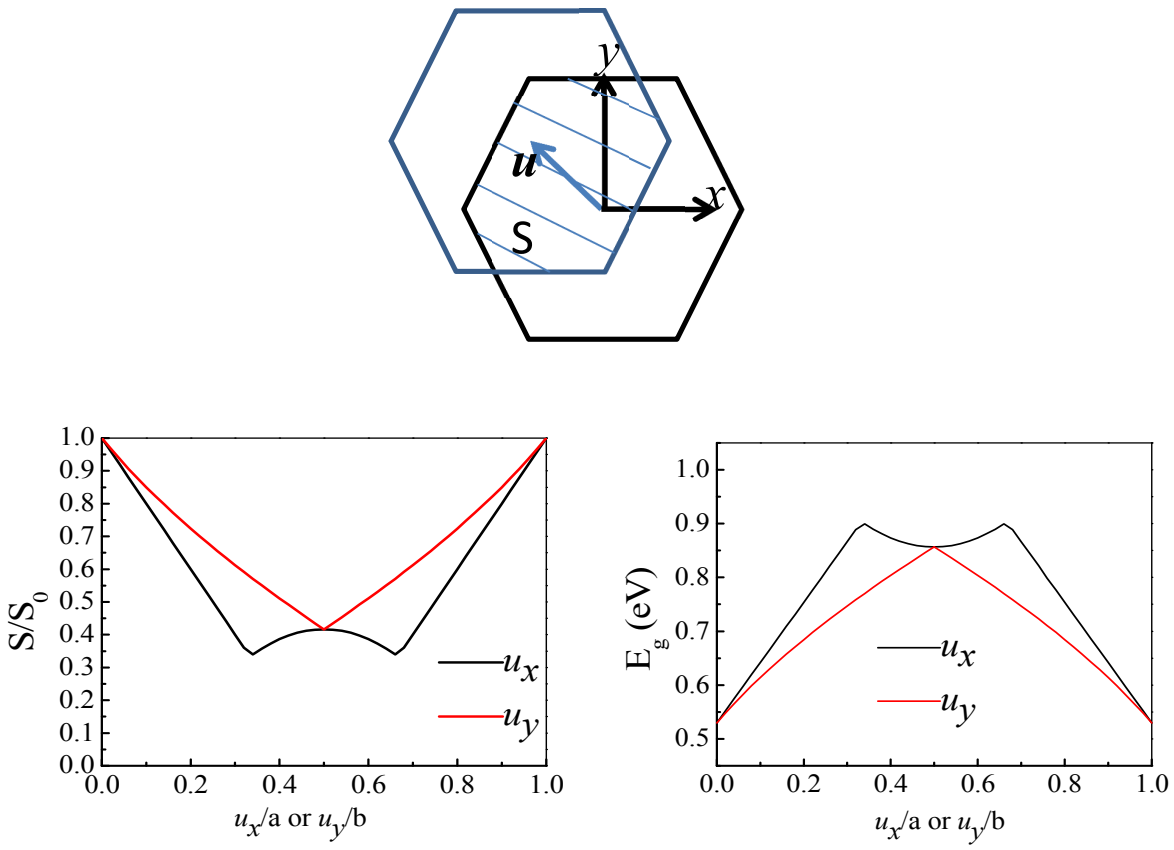

Figure S3 $S(\boldsymbol{u})$ and estimated E_g ($S(\boldsymbol{u})$) along (0,0) to (a,0) in black and (0, 0) to (0, b) in red.

An approximately linear relationship may be regressed between E_g and S,

E_g [eV] = 1.09-0.56S/S_0 (1) ,

where 1.09eV is just the band gap of a CBN monolayer. The plotted $E_g(S(\boldsymbol{u}))$ curve in black along (0,0) to (a,0) by such model can match Fig. 3a. Along (0, 0) to (0, b), however, the red curve cannot match well with Fig.3b especially around the end (0,b)--because the width of overlapping graphene domains decreases from m=9 to 7 as u_y increases from 0 to b.

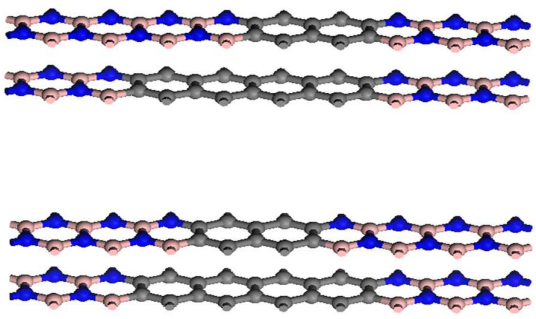

Figure S4 Two configurations of CBN bilayer with graphene domain width *n*=5 on upper layer and *n*=9 on lower layer. Here with the same graphene overlapping width *m*=5, the bandgap of upper panel with edge-edge stacking is 0.52eV, lower than 0.60eV of the lower panel. The bandgap increase of the lower panel should be caused by the decrease in the edge π-π overlapping due to the departure of nearest C_B atoms.

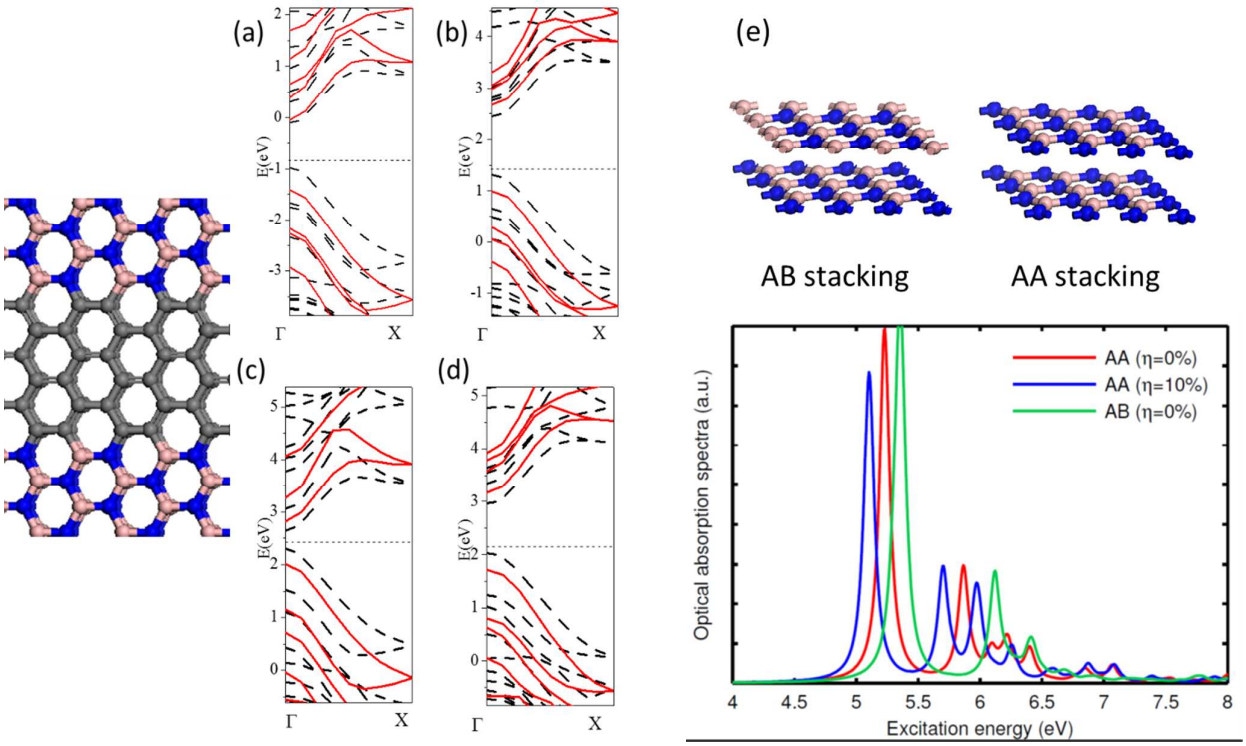

Figure S5 Bandstructures of C/BN bilayer (domain width n=4) of (a)MoM-AA and (b)IoM-AB stacking. (c)and (d) are the bandstructures of (a) and (b) after the interlayer distance decreases

by 10%. Black slash and red solid lines denote bands calculated by using PBE and HSE respectively.

(e)Optical adsorption spectrum of BN bilayer of AB and AA stacking style, and with interlayer distance compressed by 10%.